Draft version April 16, 2013
Preprint typeset using LaTeX style emulateapj v. 5/2/11

arXiv:1302.1917v2 [astro-ph.CO] 12 Apr 2013

DARK MATTER SUBHALOS AND THE X-RAY MORPHOLOGY OF THE COMA CLUSTER

Felipe Andrade-Santos[1,2], Paul E. J. Nulsen[1], Ralph P. Kraft[1], William R. Forman[1], Christine Jones[1], Eugene Churazov[3], and Alexey Vikhlinin[1]
[1]Harvard-Smithsonian Center for Astrophysics, 60 Garden Street, Cambridge, MA 02138, USA
[2]Departamento de Astronomia - IAG, Universidade de São Paulo, São Paulo - SP, Brazil and
[3]Max Planck Institute for Astrophysics, Karl-Schwarzschild str. 1, Garching D-85741, Germany
Draft version April 16, 2013

ABSTRACT

Structure formation models predict that clusters of galaxies contain numerous massive subhalos. The gravity of a subhalo in a cluster compresses the surrounding intracluster gas and enhances its X-ray emission. We present a simple model, which treats subhalos as slow moving and gasless, for computing this effect. Recent weak lensing measurements by Okabe et al. have determined masses of $\sim 10^{13}$ $M_\odot$ for three mass concentrations projected within 300 kpc of the center of the Coma Cluster, two of which are centered on the giant elliptical galaxies NGC 4889 and NGC 4874. Adopting a smooth spheroidal β-model for the gas distribution in the unperturbed cluster, we model the effect of these subhalos on the X-ray morphology of the Coma Cluster, comparing our results to *Chandra* and *XMM-Newton* X-ray data. The agreement between the models and the X-ray morphology of the central Coma Cluster is striking. With subhalo parameters from the lensing measurements, the distances of the three subhalos from the Coma Cluster midplane along our line of sight are all tightly constrained. Using the model to fit the subhalo masses for NGC 4889 and NGC 4874 gives 9.1×10^{12} $M_\odot$ and 7.6×10^{12} $M_\odot$, respectively, in good agreement with the lensing masses. These results lend strong support to the argument that NGC 4889 and NGC 4874 are each associated with a subhalo that resides near the center of the Coma Cluster. In addition to constraining the masses and 3-d location of subhalos, the X-ray data show promise as a means of probing the structure of central subhalos.

Subject headings: dark matter – galaxies: clusters: individual (A1656) – galaxies: clusters: intracluster medium – large-scale structure of the universe – X-rays: galaxies: clusters

1. INTRODUCTION

In the standard ΛCDM cosmology, the massive halos dominated by dark matter that host galaxies, groups, and clusters of galaxies assemble by mergers of smaller structures. Under the influence of gravity, uncollapsed matter and smaller collapsed halos fall into larger halos and, occasionally, halos of comparable mass merge with one another. Earlier generations of dark matter halos can survive as subhalos within the resulting aggregates, causing significant departures from the idealized smooth mass distributions often used to model dark matter halos. Hierarchical collapse models make clear predictions for the level of substructure within dark matter halos, which can provide tests of the ΛCDM model. A possible conflict with these predictions for galaxy scale dark halos is the basis of the "missing dwarf problem" (Klypin et al. 1999; Moore et al. 1999; Rocha et al. 2013).

Numerical simulations of structure formation find that many ($\sim$ 10) dark matter halos with masses of $\sim 10^{12}$ $M_\odot$ would be accreted by a rich galaxy cluster during the past few Gyr. Using the Millennium I & II simulations (Springel et al. 2005; Boylan-Kolchin et al. 2009), Fakhouri et al. (2010) find that the Coma Cluster ($M_{\rm tot} = 2 \times 10^{15}$ $M_\odot$) would have accreted $\sim$ 7 dark matter halos with masses in the range 10^{12} – 10^{13} $M_\odot$ in the last Gyr. Supporting this prediction, the analysis of Giocoli et al. (2010), which identifies substructures at all levels of the hierarchy (subhalos, sub-subhalos, etc.), finds that there should be $\sim$ 7 dark matter substructures, with masses in this range, present in a cluster like Coma today.

Recently, Churazov et al. (2012) analyzed X-ray surface brightness fluctuations in the central region of the Coma Cluster. They discuss the physical origin of these fluctuations, noting in particular that fluctuations in the gravitational potential associated with the two massive central galaxies in Coma could account for some of the larger scale surface brightness fluctuations in that region (see also Vikhlinin et al. 1994). In this paper, we present a more detailed model for the effect of subhalos, quantified by gravitational lensing measurements, on the X-ray surface brightness in the central region of the Coma Cluster.

1.1. *The Coma Cluster*

The Coma Cluster ($z = 0.0236$) has long been considered typical of dynamically relaxed systems. However, a wide range of studies have revealed that it contains complex substructure. Optical signatures of substructure come from the work of Fitchett & Webster (1987), who used a maximum likelihood method to partition the cluster into subsystems that have yet to come into dynamical equilibrium with one another, and Mellier et al. (1988), who determined mass-to-light ratios for the substructure surrounding the two dominant galaxies in the cluster core. Colless & Dunn (1996) used a sample of 552 galaxy redshifts to further clarify the merger history of the Coma Cluster. X-ray studies also reveal a remarkable complexity. Briel et al. (1992) detected diffuse X-ray emission from the regions of NGC 4839

and 4911 subgroups at 6% and 1% of the total cluster emission, respectively. White et al. (1993) showed that the Coma Cluster was formed by the merging of several distinct subunits which are not yet fully destroyed and Vikhlinin et al. (1994) showed that the extended regions of X-ray emission in the central region of Coma are associated with the subgroups NGC 4889 and 4874. Biviano et al. (1996) combined *ROSAT* and extensive optical redshift and photometric samples to identify the main body of the cluster, suggesting that it is rotating. They also concluded, based on the differences in velocity between the NGC 4889 and NGC 4874 groups and the cluster mean, that these groups only arrived recently in the cluster core. In a more recent work, Gerhard et al. (2007) used planetary nebulae as tracers to investigate the ongoing subcluster merger in the Coma core. From the planetary nebulae line of sight velocity distribution they concluded that the NGC 4889 subcluster is likely to have fallen into Coma from the eastern A2199 filament, in a direction nearly in the plane of the sky, thus colliding with the NGC 4874 subcluster coming from the west. Adami et al. (2005) presented a multi-wavelength analysis of subclustering in Coma, using X-ray data and a compilation of nearly 900 galaxy redshifts to partition the cluster into 17 subgroups that they identify as the remnants of infalling groups from the surrounding large-scale structure.

Further evidence of ongoing infall in Coma can be found in X-ray observations. For example, the linear filament to the southeast identified by Vikhlinin et al. (1997) in the Coma Cluster, which extends $\simeq 1$ Mpc from the cluster center toward NGC 4911 and NGC 4921, may be enhanced X-ray emission due to gas stripped from an infalling group or the potential perturbations caused by tidally stripped dark matter. In either case, it is transient on the dynamical time scale and so must be due to recent infall. In the radio, Brown & Rudnick (2011) have argued that a ~ 2 Mpc radio relic on the western side of the cluster is one signature of an infall shock, caused by a new, ongoing merger. If so, this merger is distinct from the one responsible for the formation of the X-ray filament.

X-ray studies of galaxy clusters provide clues to the dynamical effects of local matter concentrations on the intracluster (ICM). The hot intracluster plasma, which contains most of the baryonic mass in a rich cluster like Coma, is perturbed by infalling groups. Regions of enhanced X-ray emission define dense gas concentrations, for which there are a number of possible causes, including the gravitational effect of dark matter subhalos on the hot, diffuse gas. As mentioned, numerical simulations suggest that in the last Gyr of its history, the Coma Cluster has accreted ~ 7 dark matter halos with masses in the range $\sim 10^{12}$ – 10^{13} $M_{\odot}$, which might be detectable via their gravitational effect on the cluster gas. Such an effect has already been detected (Vikhlinin et al. 1997). However, a large-scale perturbation to the X-ray morphology has not previously been associated directly with embedded dark matter subhalos. Studies of the effect of subhalos on the gas may help us to better understand the cluster X-ray morphology and test predictions for the distribution of dark matter subhalos in clusters.

Okabe et al. (2010) have measured the projected mass distribution within $60'$ of the center of the Coma Cluster (around NGC 4874), using weak lensing data from two Subaru/Suprime-Cam fields. They detected eight subclump candidates, with a mean projected mass for seven[1] of the subclumps within the cluster equal to $7.2 \pm 1.9 \times 10^{12}$ $M_{\odot}$. In principle, analysis of the X-ray surface brightness of Coma can constrain the location of a dark matter subclump along our line of sight within the cluster. The gravity of a subhalo compresses the intracluster gas and produces an enhancement in X-ray brightness that depends on the density of the intracluster gas that surrounds the subhalo. Subhalos closer to the cluster center will cause greater brightness enhancements simply because they are embedded in denser gas. To explore this possibility, we have modeled enhancements in the X-ray surface brightness resulting from adiabatic compression of the intracluster gas caused by dark matter subhalos residing in an otherwise relaxed cluster potential.

In the following sections we present the observations of Coma used here (Section 2) and our model for estimating the enhancement in X-ray surface brightness caused by a dark matter subhalo embedded in the ICM (Section 3). In Section 4 we present the results of numerical calculations for three subhalos identified by Okabe et al. (2010), followed by a discussion in Section 5 and summary in Section 6. The cosmology assumed here has $\Omega_{\rm M} = 0.3$, $\Omega_{\Lambda} = 0.7$ and $H_0 = 70$ km s^{-1}Mpc^{-1}, implying a linear scale of 0.48 kpc arcsec^{-1} at the Coma distance of 100 Mpc.

2. X-RAY OBSERVATIONS AND DATA REDUCTION

Chandra and *XMM-Newton* observations of the Coma Cluster were used make maps of the hardness-ratio and X-ray surface brightness for comparison with the models that are discussed in detail in later sections of this paper. In this section we outline the observations analysis.

2.1. *Chandra Observations*

The core of the Coma Cluster (A1656) has been observed several times by *Chandra*, for a total exposure time on the ACIS-I and S detectors of 120 ks (ObsIDs 555, 556, 1086, 1112, 1113, 1114, 9714, 10672). The data were reduced following standard CIAO 4.4 procedures, with CALDB 4.5.3, including corrections for time dependence of the charge transfer inefficiency and gain. Data were also filtered for periods of high background and standard blank sky background files were used to obtain background images.[2] Events from individual observations were reprojected and co-added to generate combined *Chandra* images with a total exposure of 120 ks.

2.2. *XMM-Newton Observations*

From *XMM-Newton*, we used the same 0.5–2.5 keV EPIC/MOS imaging data as used by Churazov et al. (2012). In brief, *XMM-Newton* pointings covering a field of more than $1^{\circ} \times 1^{\circ}$ were combined into a single image,

[1] They quantified the contribution of background large-scale structure (LSS) to the projected mass distribution using Sloan Digital Sky Survey multi-band and photometric data, assuming a mass-to-light ratio appropriate for field galaxies. They found that one of the eight subclump candidates, which is not associated with any member galaxies, is significantly affected by LSS lensing.

[2] We note that the background level for the X-ray bright Coma Cluster is practically negligible.

the central part of which was fitted to our models. Periods of background flaring were filtered out based on the event rate above 10 keV. Background images were made by scaling "blank sky fields" to match observed count rates in the 11–12 keV band. The image area extends well outside the field covered by *Chandra*, to the outskirts of the Coma Cluster. The cleaned and calibrated MOS data were combined to make a raw 0.5–2.5 keV image, together with a background image and exposure map. An error map was computed assuming Poisson statistics for the image and background data. Simulated images are multiplied by the exposure map for fitting to the background subtracted raw image.

3. SUBHALOS IN COMA

As discussed in Section 1.1, simulations of hierarchical structure formation suggest that about seven dark matter subhalos with masses of $\gtrsim 5 \times 10^{12}\ M_\odot$ are expected to be present in the Coma Cluster now. Here we explore the observable impact of dark matter subhalos on gas near the cluster center, where their effect on the cluster X-ray emission is greatest. Using lensing data, Okabe et al. (2010) have reported the discovery of seven subclumps with masses of $\sim 10^{13}\ M_\odot$, three of which are marked in Figure 1. Two of these lie close to the giant elliptical galaxies NGC 4874 and NGC 4889, and their masses are consistent with the masses attributed to subgroups associated with these two galaxies in previous studies (subclumps 2 and 1, respectively, in Figure 1; Mellier et al. 1988; Vikhlinin et al. 1994). We begin by outlining a simple model for estimating the effect of subhalos on the X-ray surface brightness of a cluster, which we then apply to subhalos in the Coma Cluster.

3.1. *Impact on the Intracluster Gas*

We treat the subhalos as static perturbations on the large scale gravitational potential of the cluster. An off-center subhalo cannot remain at rest, but, unless its speed is comparable to the sound speed or greater, the effect of its motion on the gas is modest (e.g., see Machacek et al. 2005). The differences between the mean radial velocity of the Coma Cluster and the radial velocities of NGC 4874 and NGC 4889 are $\Delta v_r = 299$ and -430 km s^{-1}, respectively, both small compared to the gas sound speed of $\simeq 1400$ km s^{-1}. Although the transverse velocities of these galaxies are unknown, the lack of evidence for shock fronts or substantial asymmetries in the distribution of gas in their vicinities suggests that their motion through the cluster is significantly subsonic. Thus, the hydrostatic approximation is likely to be valid for the associated subhalos. More generally, the motion of typical subhalos is expected to be roughly transonic. Although transonic motion certainly alters details of perturbations to the gas density, the hydrostatic approximation will provide a good estimate for the magnitude of the change in the X-ray surface brightness, unless the speed of a subhalo is appreciably supersonic (see the Appendix).

The effect of a static subhalo is to deepen the gravitational potential locally, drawing in and compressing the gas, thereby increasing the local X-ray emission. At the relevant temperatures and for typical element abundances, the broad band responses of both *Chandra* and *XMM-Newton* to optically thin thermal emission from hot gas are relatively insensitive to the gas temperature. For example, for a fixed emission measure, the 0.5–2.5 keV count rate of the *Chandra* ACIS-I declines by a total of $\simeq 17\%$ as the gas temperature increases from $k_{\rm B}T = 4$ to 12 keV. The temperature dependence of the *XMM-Newton* response is similar. Thus, we can reasonably ignore the temperature dependence of the *Chandra* and *XMM-Newton* responses and assume that the X-ray count rate per unit volume of the gas depends only on its density, being directly proportional to the square of the gas density.

Apart from tiny cores of cool gas in NGC 4889 and NGC 4874 (Vikhlinin et al. 2001), the cooling time of the gas near the center of the Coma Cluster exceeds the Hubble time, so that the effects of radiative cooling are negligible. For a slowly moving subhalo, the response of the gas is therefore adiabatic. We assume that the perturbed region is small compared to the scale over which gas properties vary appreciably, so that the gas affected by a subhalo is approximately isentropic. The momentum equation for isentropic gas may be written

$$\frac{d\mathbf{v}}{dt} = -\nabla(H + \Phi), \tag{1}$$

where Φ is the gravitational potential, $\mathbf{v}$ is the gas velocity, $H = 5k_{\rm B}T/(2\mu m_{\rm H})$ is the specific enthalpy of the gas, T is its temperature, $\mu m_{\rm H}$ is the mean mass per gas particle, $k_{\rm B}$ is the Boltzmann constant, and the ratio of specific heats is assumed to be $\gamma = 5/3$ throughout this paper. For slow motion, we can ignore $d\mathbf{v}/dt$ to obtain

$$H + \Phi \simeq \text{constant} \tag{2}$$

at any given time. As discussed in the Appendix, Equation (2) provides a good estimate for the local perturbation due to a subhalo that moves at no more than transonic speeds and has a small mass ($GM_{\rm t}/H_0 \ll R_{\rm c}$, the cluster core radius, in the notation below). The subhalo also needs to have been well stripped of its gas, since we ignore any possible effects due to the motion through the ICM of a remaining atmosphere bound to the subhalo. This is generally a good approximation for subhalos near the center of the Coma Cluster. Note that our assumption that the perturbations are adiabatic (isentropic) differs from the assumption of isothermality employed by Churazov et al. (2012). Isentropic gas is less compressible than isothermal gas, so that a dark halo will cause a smaller change in surface brightness under the model used here (for the same perturbation, $\delta\Phi$, expanded to first-order, the change in surface brightness estimated here is 60% of that of Churazov et al. 2012).

Expressing the gravitational potential at $\mathbf{r}$ as $\Phi(\mathbf{r}) = \Phi_0(\mathbf{r}) + \delta\Phi(\mathbf{r})$, where Φ_0 is the potential of the unperturbed cluster and $\delta\Phi$ is the potential of a subhalo, the local effect of the potential perturbation is to modify the specific enthalpy to $H \simeq H_0 - \delta\Phi$, where H_0 is the specific enthalpy of the unperturbed gas at the location of interest. For locally isentropic gas with $\gamma = 5/3$, the perturbed electron density is

$$n = n_0 \left(1 - \frac{\delta\Phi}{H_0}\right)^{3/2}, \tag{3}$$

where n_0 is the unperturbed electron density at the position of interest.

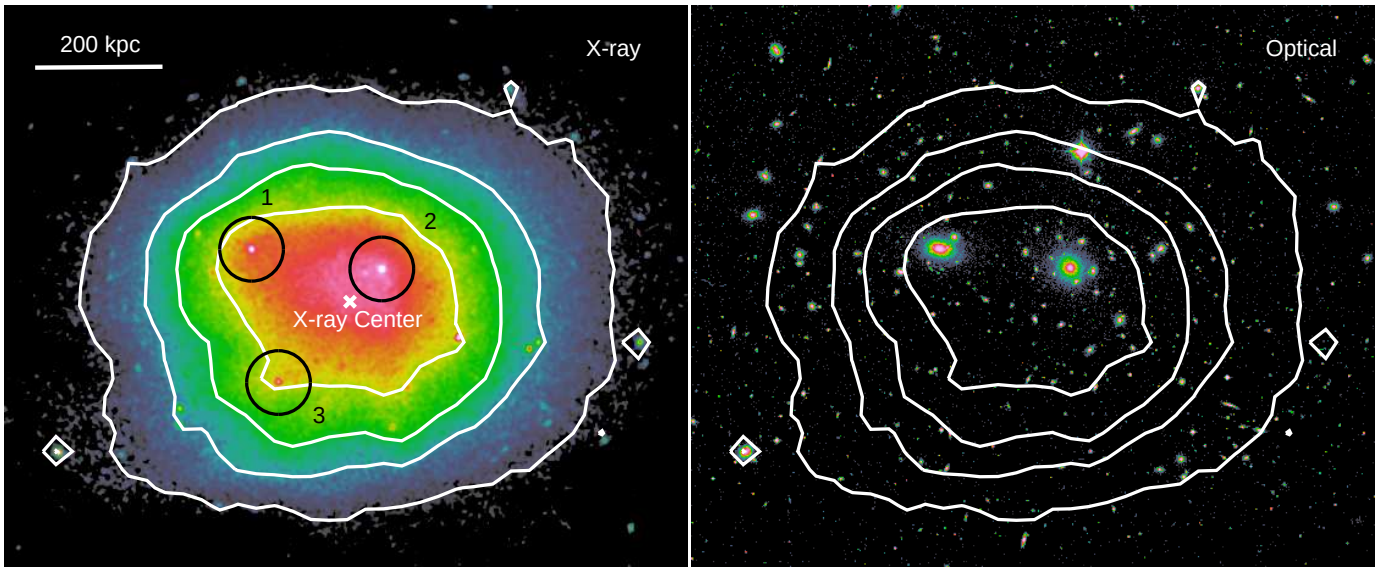

FIG. 1.— Left: positions of the three central subhalos. Subhalo 1 is centered on NGC 4889 (denoted by the number 1), subhalo 2 is centered on NGC 4874 (2), and subhalo 3, which has no optical counterpart, is centered on X-ray bright source closest to the lensing position from Okabe et al. (2010). Right: the *XMM-Newton* image contours are shown overlaid on the optical image (SAO-DSS) in the right panel.

3.2. *Conduction and the Adiabatic Approximation*

High thermal conductivity in the Coma ICM has the potential to make the perturbations more nearly isothermal than adiabatic. When the effect of a subhalo can be regarded as a first order perturbation and the gas is effectively hydrostatic, first order changes in the entropy distribution produce no first order change in the pressure. This makes the perturbations locally isobaric in the presence of thermal conduction. Including conduction in the energy equation and expanding to first order gives

$$\frac{5p_0}{2T_0}\frac{\partial \delta T}{\partial t} = \kappa_0 \nabla^2 \delta T, \tag{4}$$

where p_0, T_0, and κ_0 are the unperturbed pressure, temperature, and conductivity, respectively, and δT is the temperature perturbation. From this, we can estimate the time required for thermal conduction to turn subhalo perturbations from adiabatic to isothermal on the length scale ℓ as

$$t_{\rm cond} = \frac{5p_0\ell^2}{2\kappa_0 T_0}. \tag{5}$$

As a subhalo moves at speed v_0 through the ICM, the gas immediately around it is continually changing. The time the subhalo takes to cross a region of size ℓ is $t_{\rm cross} = \ell/v_0$. For conduction to make regions of this size isothermal, we must have $t_{\rm cond} < t_{\rm cross}$. Equating these timescales determines the approximate extent, $\ell_{\rm max}$, of the region that is kept isothermal as a subhalo moves through the ICM,

$$\ell_{\rm max} = \frac{2\kappa_0 T_0}{5p_0 v_0}. \tag{6}$$

Near the center of the Coma Cluster, the electron density is close to 0.004 cm^{-3} (Lyskova et al., in preparation), so that, for a temperature of 8 keV, the electron mean free path is $\simeq 3.7$ kpc, which is small compared to a subhalo. In the absence of a magnetic field, the thermal conductivity would be $\kappa_{\rm S} \simeq 4.2\times10^{13}$ erg cm^{-1} s^{-1} K^{-1}. The effective conductivity of the magnetized ICM is poorly known, but expressing it as $\kappa_0 = f\kappa_{\rm S}$, the largest reasonable value is $f \simeq 0.2$ (Narayan & Medvedev 2001). Scaling to these values gives

$$\ell_{\rm max} \simeq 50\ f \left(\frac{kT_0}{8\ {\rm keV}}\right)^{5/2} \left(\frac{n_0}{0.004\ {\rm cm}^{-3}}\right)^{-1} \times \left(\frac{v_0}{1000\ {\rm km\ s}^{-1}}\right)^{-1}\ {\rm kpc}. \tag{7}$$

For $f = 0.2$, this is comfortably smaller than the size of all three subhalos considered here at their best-fitting distances from the cluster center (Table 2). On scales greater than $\ell_{\rm max}$, the adiabatic approximation is more accurate than the isothermal approximation. Because the long range gravitational impact of a subhalo is most significant for its effects on the surface brightness, the adiabatic approximation is appropriate for the subhalos considered here. Ignoring the effects of conduction slightly underestimates the peak surface brightness over a subhalo. We would need to know both the effective conductivity and the speed of a subhalo to correct for this.

Note that the emission measure weighted temperature profiles in Figure 6 are quite sharply peaked and would be more significantly affected by a high effective thermal conductivity than the surface brightness profiles. Potentially, the temperature profiles can provide a probe of the effective conductivity on scales of a few tens of kpc, although existing instruments do not have the sensitivity and accuracy to use it (cf., e.g., Markevitch et al. 2003).

3.3. *Unperturbed Cluster Model*

The gas density distribution in the unperturbed cluster is assumed to have a prolate spheroidal form, with its major axis in the plane of the sky. With the z axis along our line of sight, the ellipsoidal coordinate, R, is

expressed in terms of cartesian coordinates (x, y, z), with their origin at the cluster center, by

$$\begin{cases} x' = x\cos\theta + y\sin\theta; \\ y' = x\sin\theta - y\cos\theta; \\ R^2 = x'^2 + (y'^2 + z^2)/\epsilon^2, \end{cases}$$

where θ determines the orientation of the major axis and ϵ is related to the eccentricity, e, by $\epsilon^2 = 1 - e^2$. In terms of R, the unperturbed gas density distribution is given by the β-model for the electron density,

$$n_0(R) = n_c \left[1 + \left(\frac{R}{R_c}\right)^2\right]^{-3\beta/2}, \quad (8)$$

where the central density, n_c, the core radius, R_c, and β are all constants.

The temperature plays a secondary role in our models, only entering through the unperturbed enthalpy in Equation (3). Thus, the temperature in the unperturbed cluster is assumed to be constant, an adequate approximation for the core region of the Coma Cluster (see Arnaud et al. 2001; Briel et al. 2001).

3.4. *Subhalo Model*

The density distribution of gravitating matter in a subhalo is assumed to have the NFW form (Navarro et al. 1997),

$$\rho(r) = \frac{\rho_0}{r/a(1 + r/a)^2}, \quad (9)$$

where r is the distance from the center of the subhalo, a is the scale radius, and ρ_0 is the scale density. The subhalo density profile is truncated at $r = r_t$, giving a total mass of

$$M_t = 4\pi\rho_0 a^3 \left[\ln(1 + w_t) - \frac{w_t}{1 + w_t}\right], \quad (10)$$

where $w_t = r_t/a$. The corresponding gravitational potential perturbation is

$$\delta\Phi(r) = \begin{cases} 4\pi G\rho_0 a^2 \left[\dfrac{1}{1 + w_t} - \dfrac{a}{r}\ln(1 + r/a)\right], & r \le r_t \\ -\dfrac{GM_t}{r}, & r > r_t. \end{cases} \quad (11)$$

The densities of the subhalos determined by Okabe et al. (2010) from lensing data are higher than expected from simple hierarchical collapse models. Using the NFW model, we can estimate the properties of a progenitor halo from those of its remnant subhalo. If the subhalo was simply truncated by falling into the cluster, its mass, M_t, size, r_t, and scale length, a, determine the scale density, ρ_0, of its progenitor through Equation (10). In terms of the mean density of the subhalo, this requires

$$\begin{aligned} \overline{\rho}_t &= \frac{3M_t}{4\pi r_t^3} = \rho_0 \left[\frac{3}{w^3}\left\{\ln(1 + w) - \frac{w}{1 + w}\right\}\right]_{w = r_t/a} \\ &= \rho_0 F(r_t/a), \end{aligned} \quad (12)$$

which determines ρ_0 as well as defining the form of $F(w)$. To estimate the virial radius of the progenitor halo, we adopt the usual approximation that the mean density within the virial radius is 200 times the critical density, evaluated at the redshift of the Coma cluster. That is, the virial radius of the progenitor, r_{vir}, is determined by solving

$$\overline{\rho}_{vir} = 200\frac{3H^2}{8\pi G} = \rho_0 F(r_{vir}/a) = \overline{\rho}_t F(r_{vir}/a)/F(r_t/a), \quad (13)$$

where Equation (12) has been used to eliminate ρ_0. Here only, H is the Hubble constant at the redshift of the Coma Cluster (not the specific enthalpy). The virial mass is then $4\pi\overline{\rho}_{vir} r_{vir}^3/3$, an increasing function of r_{vir}. For example, for a subhalo with a mass of $10^{13}\ M_\odot$ enclosed within $r_t = 50$ kpc, if its scale radius is $a = 50$ kpc, the concentration parameter, $c = r_{vir}/a$, of the progenitor group would have been $\simeq 19.4$ ($r_{vir} \simeq 970$ kpc) and its total mass would have been $\simeq 1.07 \times 10^{14}\ M_\odot$. Reflecting the high density of the subhalo, a concentration parameter of 19.4 is higher than expected for such a massive progenitor (e.g., Mandelbaum et al. 2008). Since the NFW scale lengths of the subhalos are largely unconstrained, this issue might be remedied by a different value for a. Differentiating Equation (13) with respect to a gives the dependence of r_{vir} on a as

$$\left[\frac{d\ln F(w)}{d\ln w}\right]_{w = r_{vir}/a} \frac{d\ln r_{vir}}{d\ln a} = \left[\frac{d\ln F(w)}{d\ln w}\right]_{w = r_{vir}/a} - \left[\frac{d\ln F(w)}{d\ln w}\right]_{w = r_t/a} \quad (14)$$

and, from the definition of F,

$$\left[\frac{d\ln F(w)}{d\ln w}\right]_{w = r/a} = 3\left[\frac{\rho(r)}{\overline{\rho}(r)} - 1\right], \quad (15)$$

where $\overline{\rho}(r)$ is the mean density of an NFW halo inside radius r, so that

$$\left[\frac{\rho(r_{vir})}{\overline{\rho}(r_{vir})} - 1\right]\frac{d\ln r_{vir}}{d\ln a} = \frac{\rho(r_{vir})}{\overline{\rho}(r_{vir})} - \frac{\rho(r_t)}{\overline{\rho}(r_t)}. \quad (16)$$

Now $\rho(r)/\overline{\rho}(r) < 1$ and, for an NFW halo, $\rho(r)/\overline{\rho}(r)$ is a decreasing function of r, so that Equation (16) shows that r_{vir} is an increasing function of a. It follows that the virial mass determined from the subhalo properties is an increasing function of a. Expressing r_{vir} as $r_{vir} = ca$, where c is the concentration parameter, Equation (16) also shows that c is a decreasing function of a. The progenitor mass cannot be less than the subhalo mass $M_t = 10^{13}\ M_\odot$ and a concentration parameter of 19.4 is already too high for that mass, so reducing a, which would increase the concentration parameter, cannot give a consistent progenitor mass and concentration parameter. Increasing a does not help either. Raising a to 288 kpc would make the progenitor mass $10^{15}\ M_\odot$, with a concentration parameter of 7.1, which is also too high for the halo mass. Since this progenitor mass is already about half the total mass of the Coma Cluster (e.g., Kubo et al. 2007), it is unreasonable for the progenitor to be any more massive. This leaves no reasonable parameters for the progenitor consistent with expectations for standard ΛCDM structure formation models.

So far, we have assumed that the remnant subhalos are simply truncated by falling into the cluster, but it

is far more likely that the mean density of a subhalo is reduced by its interactions with the cluster. Allowing for this would require even greater mean densities for the progenitors, exacerbating the issue of the high subhalo densities. Thus, the subhalos defined by Okabe et al. (2010) are smaller than expected from standard structure formation models, if they fell into the Coma Cluster in the recent past. The simplest resolution to this issue would be if the more massive central subhalos fell into Coma long in the past, when the mean densities of their progenitors would have been higher (cf. Biviano et al. 1996). Our results are much less sensitive to the structure of a subhalo than they are to its total mass, so we do not pursue this issue any further here.

3.5. *Estimate for the Effect of a Subhalo*

With the approximations outlined above, the perturbation to the X-ray surface brightness must still be computed numerically (Section 4). However, before considering the numerical results, we make a crude estimate of the effect on the X-ray surface brightness of a single subhalo. Under our assumptions, the fractional change in X-ray surface brightness is

$$\frac{\delta I}{I} = \frac{\int (n^2 - n_0^2) dz}{\int n_0^2 dz}, \tag{17}$$

where the integrals are along the line of sight. To first order in $\delta\Phi$, Equation (3) gives $n^2 - n_0^2 \simeq n_0^2(-3\delta\Phi/H_0)$. For a localized perturbation, we get the further approximation,

$$\begin{aligned}\int (n^2 - n_0^2) dz &\simeq 3n_0^2/H_0 \int_{-z_{\rm max}}^{z_{\rm max}} -\delta\Phi dz \\ &\simeq 6n_0^2 \frac{GM_{\rm t}}{H_0} \ln\left[\frac{z_{\rm max}}{\varpi} + \sqrt{1 + \left(\frac{z_{\rm max}}{\varpi}\right)^2}\right], \end{aligned} \tag{18}$$

where ϖ is the minimum distance of the line of sight from the center of the subhalo and this result applies to lines of sight with $\varpi > r_{\rm t}$. The integration has been truncated at $z = \pm z_{\rm max}$ to avoid a logarithmic divergence (a spurious consequence of the crude approximations used here). For lines of sight that intersect the subhalo, i.e., for $\varpi \leq r_{\rm t}$, the magnitude of the result is similar. Setting the logarithmic factor to unity and using the form (8) for the unperturbed ICM density, n_0, finally gives us an order of magnitude estimate for the fractional perturbation in the surface brightness near the center of the subhalo

$$\frac{\delta I}{I} \simeq \frac{6GM_t}{R_{\rm c} H_0 B(3\beta - 1/2, 1/2)} \times \frac{R_{\rm c}(R_{\rm c}^2 + \varpi_{\rm p}^2)^{3\beta - 1/2}}{(R_{\rm c}^2 + \varpi_{\rm p}^2 + z_{\rm p}^2)^{3\beta}}, \tag{19}$$

where $B(a, b)$ is the β function, and $\varpi_{\rm p}$ and $z_{\rm p}$ are cylindrical coordinates for the center of the subhalo measured with respect to the cluster center, i.e., their projected separation and their separation along our line of sight, respectively (Figure 2). For an unperturbed gas temperature of $k_{\rm B}T_0 = 8$ keV, a subhalo mass of $M_t = 10^{13}\ M_\odot$, and β-model core radius of $R_{\rm c} = 300$ kpc, the first factor on the right in Equation (19) is $\simeq 0.17$ for $\beta \simeq 2/3$. Thus, such a subhalo should be detectable in X-ray observations, unless it is far from the cluster center ($|z_{\rm p}|$ or $\varpi_{\rm p} \gg R_{\rm c}$). Note that the estimate for $\delta I/I$ in Equation (19) only depends on the mass of a subhalo, not on its size or scale parameters. This reflects the insensitivity of the full, numerical results to details of the mass distribution in the subhalos. It is a consequence of the long range of the gravitational force.

4. SIMULATED X-RAY IMAGES OF THE COMA CLUSTER

In this section we present numerical results, employing the model outlined above to compute the effects of subhalos on the X-ray surface brightness of the Coma Cluster. The X-ray surface brightness is computed by integrating the square of the gas density, n, given by Equation (3), along lines of sight through a model cluster with an unperturbed gas temperature of $k_{\rm B}T_0 = 8$ keV and an unperturbed gas density profile given by the β-model (Section 3.3). Most parameters of the β-model are determined in the fits, as outlined below. Gas densities are evaluated and integrated numerically on a rectangular parallelepiped of $321 \times 321 \times 1000$ cubic cells, 1.906 kpc on a side and centered on the cluster. The long axis of the grid is parallel to the line of sight.

Subhalos are modeled with NFW profiles (Section 3.4), using parameters from Okabe et al. (2010). In the following analysis, apart from Section 4.2, the NFW scale radius, a, is set to 50 kpc in a subhalo that is also truncated at $r_{\rm t} = 50$ kpc to be consistent with the lensing results. The magnitude of the change in surface brightness due to a subhalo increases with the density of the surrounding gas, so that it is maximized when the subhalo is closest to the cluster midplane, defined by $z_{\rm p} = 0$. Because the effect of a subhalo is sensitive to its distance from the midplane, we can constrain the locations of the subhalos along our line of sight.

4.1. *Fitting*

Models are multiplied by the exposure map and added to the background image for fitting to the raw 0.5–2.5 keV *XMM-Newton* image of the central part of the Coma Cluster, made from the combined EPIC MOS data. Goodness of fit is determined using χ^2 as the fit statistic. The image was binned into $2'' \times 2''$ pixels and the region fitted had an extent of $10'.7 \times 10'.7$. The error estimate for each pixel includes Poisson errors for the raw image and for the background data. The fit was masked to exclude point sources evident in the *XMM-Newton* image (Figure 2). Away from point sources, the average photon count per pixel in the raw image varies from over 50 near the center to about 8 at the periphery.

Models include the three subhalos marked in Figure 1. The centers of the subhalos corresponding to the giant elliptical (gE) galaxies NGC 4889 and NGC 4874 were placed on the sky at their respective optical centers, rather than at the locations determined from the lensing data of Okabe et al. (2010). The center of subhalo 3 was placed at the location of the X-ray bright source closest to the lensing position, since the X-ray surface brightness is elongated toward this position. The lensing positions are consistent with these positions, within the errors of the lensing measurements, but using the latter positions gives somewhat better fits ($\Delta\chi^2 \simeq 700$, Table 2). Coordinates used for the subhalo centers are, for NGC 4889 (J2000) = $(195.034°, 27.977°)$, for NGC 4874, $(194.899°, 27.959°)$, and for the southern mass concentration, $(195.006°, 27.855°)$. Fixed parameters for the

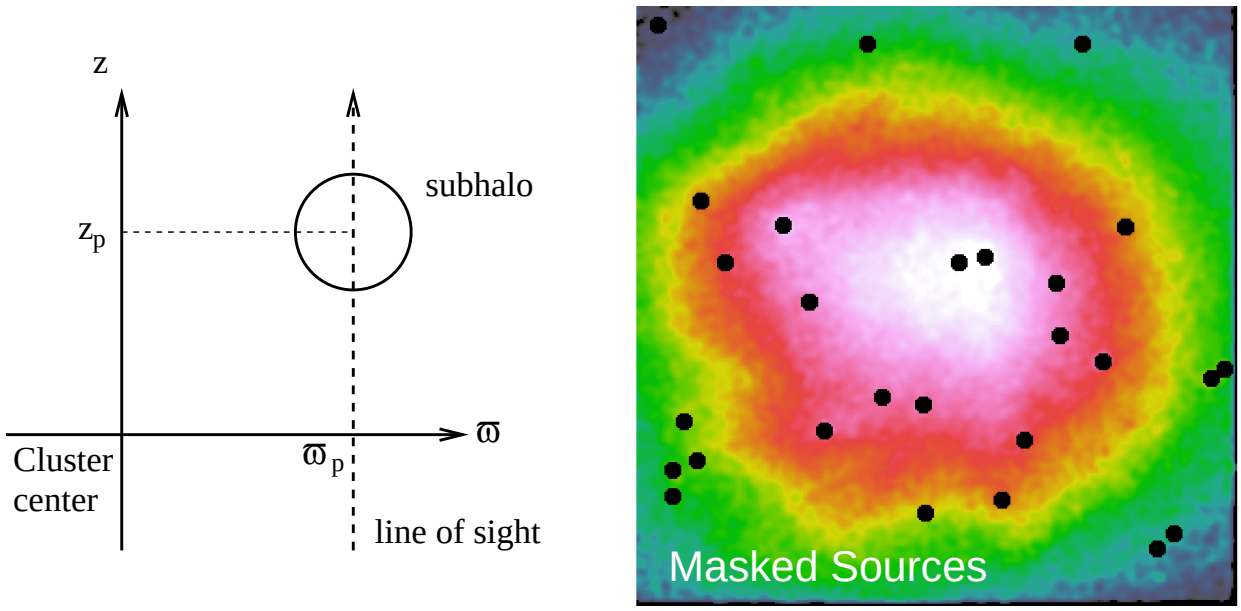

FIG. 2.— Left: parameters defining the location of a subhalo. Right: XMM-Newton image showing the mask used to remove the point sources.

TABLE 1
PARAMETERS OF SUBHALO MODELS

Subhalo	α_{J2000} (deg)	δ_{J2000} (deg)	M_t (10^{12} $M_\odot$)	a (kpc)	r_t (kpc)
1, NGC 4889	195.034	27.977	11.0	50	50
2, NGC 4874	194.899	27.959	6.57	50	50
3	195.006	27.855	7.57	50	50

subhalo models are given in Table 1. The location of the center of the X-ray emission from the Coma Cluster was determined by fitting a circularly symmetric β-model to the central region of the cluster. This center, $(194.932°, 27.929°)$, was kept fixed in all subsequent fits. All other parameters for the cluster β-model (θ, ϵ, R_c, β, normalization) are determined in the fits. For each subhalo, the only free parameter is its location along our line of sight, measured by its distance from the cluster midplane (z_p in Figure 2).

Fitting models with up to eight nonlinear, free parameters with $\sim 10^5$ degrees of freedom (dof) presented some challenges. To ensure that the global best fit was found, two different fitting procedures, a Levenberg-Marquardt algorithm (Bevington & Robinson 2003) and a grid search, were employed to cross check one another. Initially, the three subhalos were placed at $z = 1$ Mpc, effectively removing them from the fit, and the best fitting parameters for the β-model alone were determined. This fit gives $\beta = 0.80$, $R_c = 351$ kpc, $\epsilon = 0.83$, $\theta = -3.9°$, and $\chi^2 = 139204.6$, or a reduced χ^2 (χ^2/dof) of 1.3881 (Table 2).

When the three subhalos are included in the fit, with subhalos 1 and 2 at the locations of the two gE galaxies, allowing the positions along the line of sight of the three subhalos, z_i for $i = 1, 2, 3$, to vary simultaneously gives the best fitting parameters $z_1 = 121$ kpc, $z_2 = 7.9$ kpc, $z_3 = 399$ kpc, $R_c = 387$ kpc, $\theta = -0.1°$, $\epsilon = 0.84$, for which $\chi^2 = 119114.7$, making the reduced chi squared χ^2/dof $= 1.1878$. The improvement in the fit, of $\Delta\chi^2 = 20089.9$ for the addition of three parameters, is highly significant. Visual comparison of the model and cluster images in Figure 3 shows that the subhalos, particularly the two associated with NGC 4889 and NGC 4874, make the model X-ray image very similar to the observed cluster. Using $\Delta\chi^2 = 2.706$ to estimate confidence ranges for the three subhalo positions, with all of the other fitted parameters free, gives 90% confidence ranges of $z_1 = 121 \pm 5$ kpc, $z_2 = 7.9 \pm 7.5$ kpc, and $z_3 = 399 \pm 10$ kpc.

4.2. *Structure and Masses of the Subhalos*

As discussed in Section 3.4, the subhalo properties determined from the lensing measurements give them higher densities than expected for hierarchical collapse models. To test how sensitive our results are to the structure of the subhalos, we varied the truncation radius of the most massive subhalo, corresponding to NGC 4889 (subhalo 1), while its mass was kept fixed. Since the NFW model is unlikely to be valid for a truncation radius, r_t, smaller than the NFW scale length, a, we tied these two parameters together for these fits ($a = r_t$). All parameters for the other subhalos were frozen at their best-fitting values, since the fits are not sensitive to these. The resulting χ^2 and positions along our line of sight for subhalo 1 are plotted against r_t in Figure 4. The fit is clearly affected by the structure of this subhalo, with a moderately significant improvement of $\Delta\chi^2 \simeq 4$ for the best fit. However, at 47 kpc, the best fitting truncation radius for subhalo 1 is actually smaller than the value of 50 kpc from the lensing results, only exacerbating the problems caused by the high density of this subhalo (Section 3.4). This result depends on our model through properties that are not well determined, so it should be treated with caution. For example, Table 2 shows that the best fitting position, z_1, for the NGC 4889 subhalo is quite sensitive to the position on the sky of this subhalo. Nevertheless, the fact that the subhalo structure has an appreciable effect on the fit shows that the X-ray data

TABLE 2
Parameters of X-Ray Surface Brightness Model

Model[a]	β	ϵ	θ^b (deg)	R_c (kpc)	z_1 (kpc)	z_2 (kpc)	z_3 (kpc)	dof	χ^2
Cluster only[c]	0.80	0.83	-3.9	351	1000	1000	1000	100283	139204.6
Subhalos (lensing)[d]	0.82	0.84	3.2	395	39	5.8	361	100280	119817.0
Subhalos (gE)[e]	0.80	0.84	-0.1	387	121	7.9	399	100280	119114.7

Note. — [a]Using the cluster β-model of Section 3.3 and subhalo models of Section 3.4. [b]Position angle of the major axis, increasing north of west. [c]Subhalos fixed at 1 Mpc from the cluster midplane. [d]Subhalos positions on our line of sight free to vary, with the subhalos centered at the lensing positions. [e]As for *d*, but with subhalos 1 and 2 centered at the positions of the two gE's and subhalo 3 centered on the X-ray bright source.

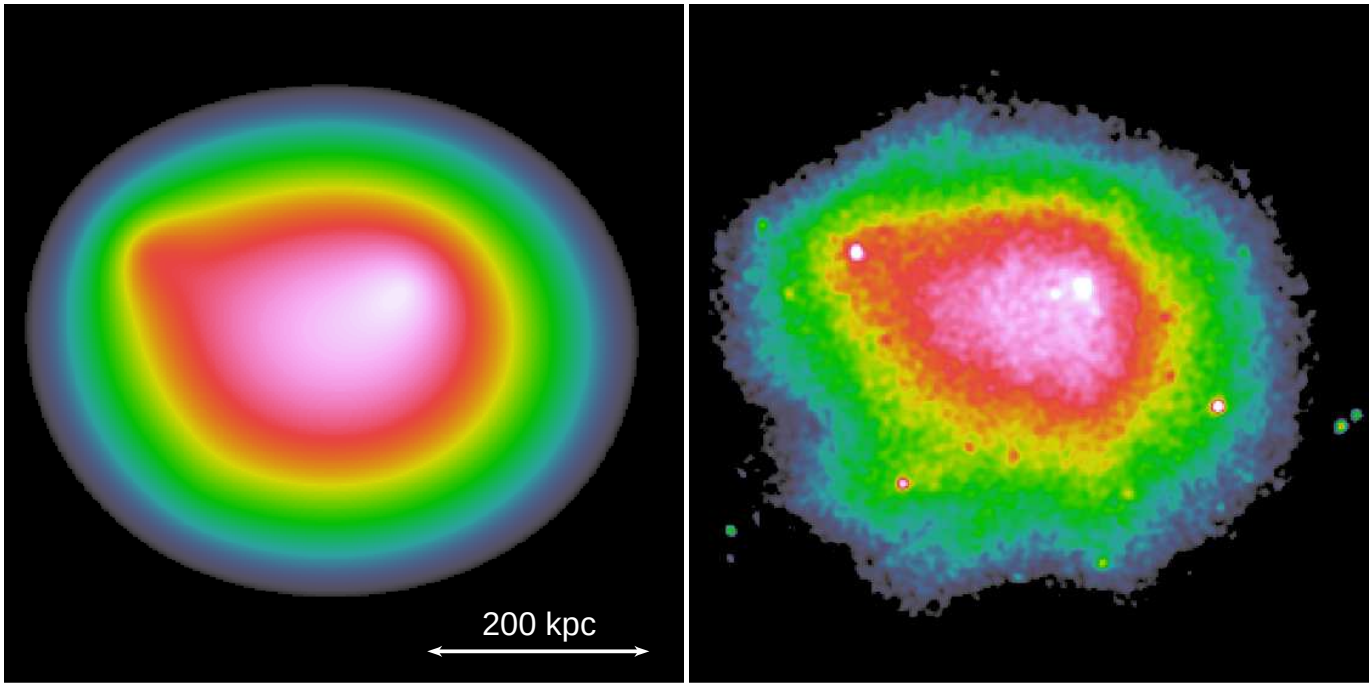

Fig. 3.— Left: Model X-ray image for the Coma Cluster, made by embedding three dark matter subhalos in the elliptical β-model of Section 3.3. Right: 0.5–4 keV *XMM-Newton* X-ray image of the Coma Cluster. North is up and east to the left. Increased brightness due to the presence of the subhalos elongates the model image in the direction of each subhalo, particularly toward the east. These features correspond well to structure in the X-ray image.

could potentially be used to probe its structure. Results for the NGC 4874 subhalo are similar.

From Section 3.5, the X-ray surface brightness of the model cluster is expected to be considerably more sensitive to the total mass of a subhalo than to its structure. In principle, we can determine the subhalo masses by fitting the X-ray image, using data that is completely independent of the lensing mass measurements. To investigate the agreement between the lensing and X-ray mass determinations, we have again used subhalo models with $a = r_t$ allowed to vary, but here the scale density, ρ_0, or, equivalently, the mean density of the subhalo, is kept fixed, so that its mass varies as $\propto r_t^3$. Parameters for the cluster model are free to vary, but those for the other subhalos are kept fixed at their best-fitting values (last row of Table 2).

The left panel of Figure 5 shows results for varying the mass of the NGC 4889 subhalo (subhalo 1). Plotted against r_t, the subhalo mass is given in the bottom panel, distance from the cluster midplane in the middle panel, and χ^2 in the top panel. Reducing the mass of the subhalo decreases its impact on the gas, hence the X-ray surface brightness, but this can be offset by shifting the subhalo toward the Coma Cluster midplane, where the unperturbed gas density is greater. The best-fitting mass for subhalo 1 is 9.14×10^{12} $M_\odot$, $\simeq 1.2\sigma$ lower than the lensing mass of Okabe et al. (2010). The corresponding improvement in the fit is $\Delta\chi^2 \simeq 237$. Results for varying the mass of the NGC 4874 subhalo are shown in the right panel of Figure 5. Here, the best fitting mass of 7.61×10^{12} $M_\odot$ is $\simeq 0.9\sigma$ greater than the lensing mass and the improvement in the fit is $\Delta\chi^2 \simeq 242$ (see Table 3). This subhalo starts from much closer to the cluster midplane than subhalo 1 and the nonmonotonic variation of z_2 seen in the plot results from the interplay between the subhalo and cluster parameters (θ and ϵ in particular, see Section 3.3). The mass of subhalo 3 also affects the fit significantly, but χ^2 continues to improve as it is increased well beyond the range consistent with the lensing data (e.g., doubling the subhalo mass moved it to

$z_3 \simeq 510$ kpc from the midplane and an improvement of $\Delta\chi^2 \simeq 350$). This indicates that our model assumptions are poorer for this subhalo.

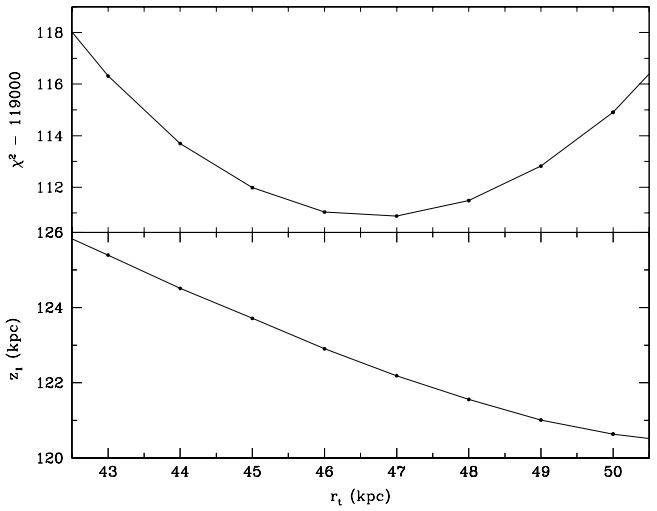

FIG. 4.— Effect of varying the truncation radius of subhalo 1. This plot shows how the fit depends on the structure of subhalo 1, through its truncation radius, r_t. The lower panel shows the best fitting distance of the subhalo from the cluster midplane along our line of sight, while the upper panel shows $\chi^2 - 119000$. For these fits, the scale radius of the subhalo, a, is tied to its truncation radius, r_t, the subhalo mass is fixed and the parameters of the other subhalos are frozen. The remaining fit parameters are free.

4.3. *Temperature Perturbations*

Next to the gravitational effect of subhalos, the most likely cause of large-scale enhancements in the X-ray surface brightness of the Coma Cluster is low entropy gas that has fallen in during the ongoing collapse. In that case, the pressure of the gas responsible for the excess emission would be similar to that of its surroundings, but its density would be higher, boosting the X-ray brightness. By contrast, gas compressed adiabatically in the potential of a subhalo should be hotter than its surroundings. For the model used here, the temperature enhancement due to adiabatic compression can be determined from $H = H_0 - \delta\Phi$ (Equation (2)). Using the emission measure weighted temperature to estimate the fractional temperature perturbation, the model gives

$$\frac{\delta T}{T_0} = \frac{\int n^2 H\, dz}{H_0 \int n^2\, dz} - 1 \simeq \frac{\int n_0^2(-\delta\Phi/H_0)dz}{\int n_0^2 dz} \simeq \frac{1}{3}\frac{\delta I}{I}, \quad (20)$$

where the third form is obtained by expanding to first order in $\delta\Phi/H_0$, using Equation (3), and the last form is obtained in the same manner from the expression for the surface brightness fluctuations in Equation (17). Combining this result with the rough estimate for $\delta I/I$ from Section 3.5, the maximum temperature fluctuation due to a subhalo is expected to be roughly 5%. Evaluated numerically for the best-fitting parameters in the last line of Table 2, the maximum temperature rise is only about 3% for NGC 4889 and less for the other two subhalos (Figure 6). These are not large enough to detect in small regions with the current data, particularly at the relatively high temperature of the Coma Cluster.

However, we can check for signatures of cooler gas that might be responsible for the enhanced X-ray emission. For this purpose, we have made maps of the hardness ratio in 50 kpc regions around each of the subhalo locations by binning *Chandra* data for the bands 0.3–1.5 keV and 1.5–6.0 keV into $15\farcs74 \simeq 7.5$ kpc pixels. The images in Figure 7 show (hard − soft)/(hard + soft). Apart from the innermost pixels for NGC 4889 and NGC 4874, there is no indication of cooler gas in any of the subhalos. Vikhlinin et al. (2001) showed that there are $\simeq 3$ kpc cores of 1–2 keV gas in both of these gE galaxies, which affect the central pixel of the respective hardness-ratio images. These regions are masked out of the image used to fit the models and they certainly do not account for the extended regions of enhanced X-ray emission associated with the subhalos. There are no other signs of cooler gas in the images of Figure 7, consistent with previous investigations (Arnaud et al. 2001; Briel et al. 2001; Neumann et al. 2003). In particular, there is no sign of a radial temperature increase in any of these regions. Apart from the solitary low pixels for the two cool cores, the histograms of the hardness ratio for each of these regions are reasonably consistent with a constant value. This is illustrated in Figure 8, which shows histograms of the hardness ratio for the regions around NGC 4889 (left panel and panel b) and NGC 4874 (right panel and panel c) in Figure 7. Statistical noise in the soft and hard counts contributes to the standard deviation of the hardness ratio as

$$\sigma_{\rm HR,stat} \simeq \frac{2\sqrt{h^2\sigma_s^2 + s^2\sigma_h^2}}{(h+s)^2}, \quad (21)$$

where s and h are the mean counts for the soft and hard bands, respectively, and σ_s and σ_h are the respective standard deviations for the two bands. Dashed lines in Figure 8 show Gaussians with means, $\mu_{\rm HR}$, equal to the data mean and normalized to match the number of samples with standard deviations given by Equation (21). The plotted number of samples per bin is given by

$$N_{\rm samples} = \frac{Nw}{\sigma_{\rm HR,stat}\sqrt{2\pi}} \exp\left(-\frac{(\psi - \mu_{\rm HR})^2}{2\sigma_{\rm HR,stat}^2}\right), \quad (22)$$

where ψ is the hardness ratio, N is the total number of samples, and w is the width of the histogram bins. The agreement between these Gaussians and the histograms shows that, apart from the single cool pixel in each core, the histograms show little evidence for variation of the hardness ratio over each subhalo.

5. DISCUSSION

Under our model assumptions, the distances from the cluster midplane of each of the three central subhalos are well constrained at the 90% confidence level ($z_1 = 121 \pm 5$ kpc, $z_2 = 7.9 \pm 7.5$ kpc and $z_3 = 399 \pm 10$ kpc), providing useful information on their three-dimensional locations within the Coma Cluster (Section 4.1). In particular, subhalo 1 (NGC 4889) is closer to the cluster midplane than its distance from the cluster center and subhalo 2 (NGC 4874) is even closer to the cluster midplane. By contrast, subhalo 3 is 1.7 times further from the midplane than it is from the cluster center. These results are affected by our model assumptions, particularly those concerning the masses and locations on the

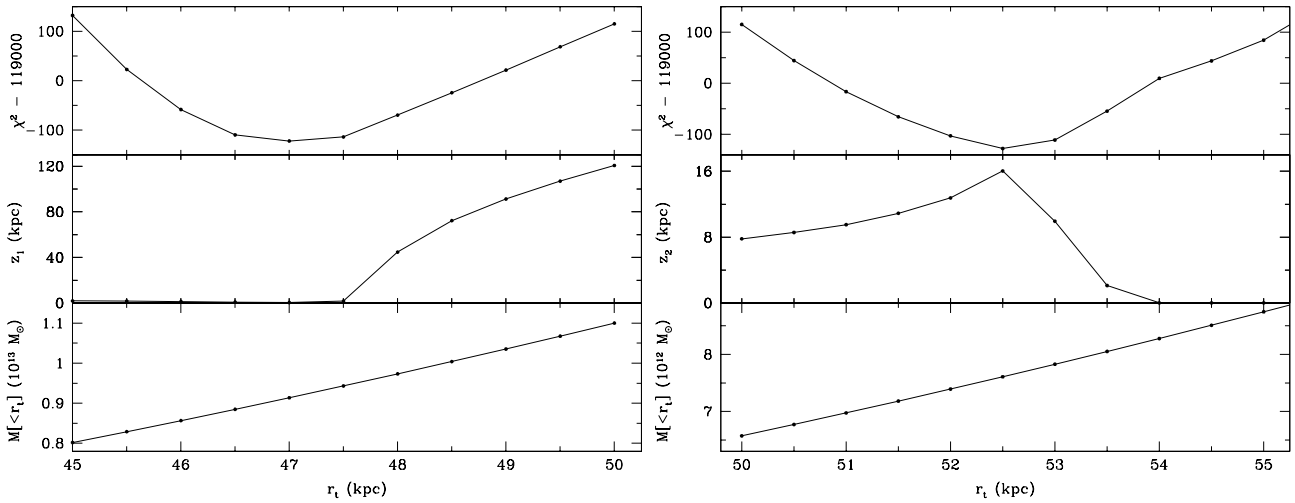

FIG. 5.— Effect on the fit of varying subhalo mass. Left: Fit results for the NGC 4889 subhalo are plotted against its truncation radius, $r_{\rm t}$, with the mean density of the subhalo held constant. Right: same for NGC 4874. The bottom panels show the subhalo mass ($\propto r_{\rm t}^3$), the middle panels show its position along our line of sight, and the top panels show $\chi^2 - 119000$. Model parameters match the lensing parameters in Table 1 for $r_{\rm t} = 50$ kpc. For these fits, the scale radius of the subhalo, a, is tied to its truncation radius, $r_{\rm t}$, the mean density of the subhalo is fixed, while the parameters of the other subhalos are frozen.

TABLE 3
BEST-FIT MASSES OF THE SUBHALOS

Subhalo	$\alpha_{\rm J2000}$ (deg)	$\delta_{\rm J2000}$ (deg)	$M_{\rm t}$ (10^{12} $M_\odot$)	a (kpc)	$r_{\rm t}$ (kpc)	$\Delta\chi^2$
1, NGC 4889	195.034	27.977	9.1	47	47	237
2, NGC 4874	194.899	27.959	7.6	52.5	52.5	242

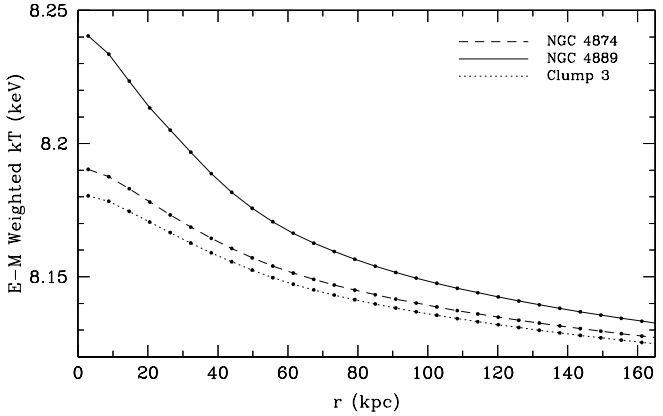

FIG. 6.— Emission measure weighted temperature profiles computed from our model for the three subhalos. The peak temperature over the NGC 4889 subhalo is 3% greater than the model temperature of 8 keV.

sky of the subhalos. They are also affected by our largely arbitrary assumption that the gas distribution in the unperturbed cluster is prolate, with its major axis in the plane of the sky. While these assumptions affect the distances of the subhalos from the cluster midplane, they do not alter the qualitative result that subhalos 1 and 2 lie close to the cluster midplane, while subhalo 3 does not. Our results are consistent with previous findings that NGC 4889 and NGC 4874 lie close to the cluster center (e.g. Biviano et al. 1996).

Nonlinearity, from Equations (3) and (17), means that the impact of two or more subhalos on the X-ray surface brightness increases when they are closer together. As a result, the placement of subhalos about the cluster midplane can alter the fit. This is seen in the fit results for subhalos 1 and 2. In computing the confidence range for subhalo 2, we found that $\Delta\chi^2$ continues to rise as z_2 decreases through zero. In principle, the fit should be symmetric about $z_2 = 0$, but, to enforce that result it would be necessary to flip the positions of the other subhalos to the opposite side of the cluster midplane as subhalo 2 crossed the midplane. This behavior shows that the fit is better (formally, at the 90% level) when subhalos 1 and 2 lie on the same side of the cluster midplane. Of course, this does not determine which side of the midplane that is. Subhalo 3 is too far from the other two subhalos to obtain any information about its location relative to them.

When the masses of the subhalos were allowed to vary (Section 4.2), the best fitting masses for the subhalos associated with the two gE galaxies near the cluster center ($m_1 = 9.1 \times 10^{12}$ $M_\odot$ and $m_2 = 7.6 \times 10^{12}$ $M_\odot$) were found to be consistent with their lensing masses ($m_{1,\rm lens} = (11.0 \pm 1.5) \times 10^{12}$ $M_\odot$ and $m_{2,\rm lens} = (6.6 \pm 1.2) \times 10^{12}$ $M_\odot$), though not for subhalo 3. Formally, the large improvements in the fit show that the X-ray masses determined for the NGC 4889 and NGC 4874 subhalos would be much more accurate than the lensing masses. However, given the shortcomings of our model, particularly the approximation that the subhalos are static, the results would be dominated by systematic uncertainties. More accurate and more realistic models are required to assess the systematics, so we make no attempt to pursue this further here. The remarkable consistency between

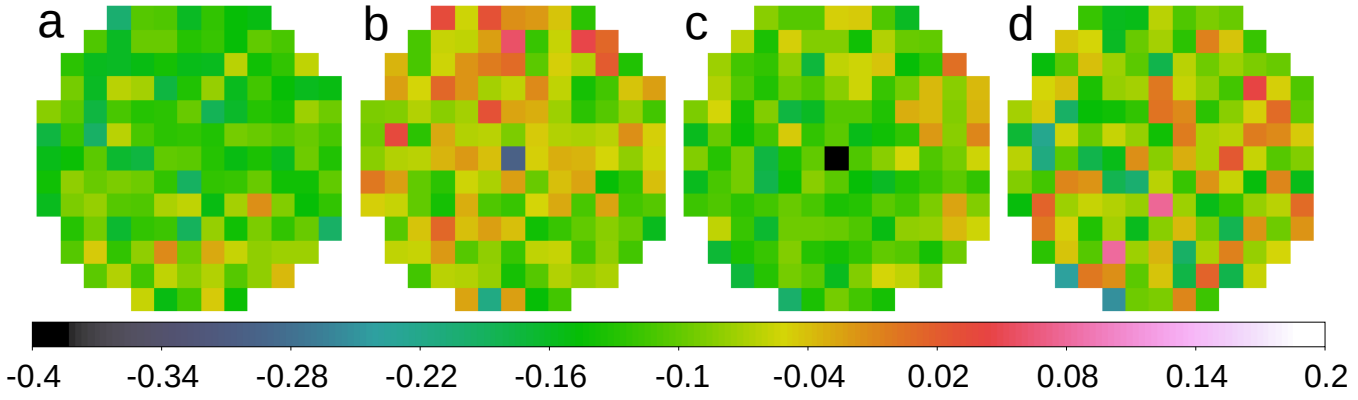

FIG. 7.— Hardness-ratio maps for the subhalos. *a)* a representative region lying between the 3 subhalos. *b)* subhalo 1, centered on NGC 4889. *c)* subhalo 2, centered on NGC 4874. *d)* subhalo 3, centered on the X-ray bright source. The hardness ratio is defined in the text. Each map covers a region $102''$ or $\simeq 50$ kpc in radius. Apart from the single cool central pixels for NGC 4889 and NGC 4874, there is no significant sign of a radial temperature gradient in any of these regions.

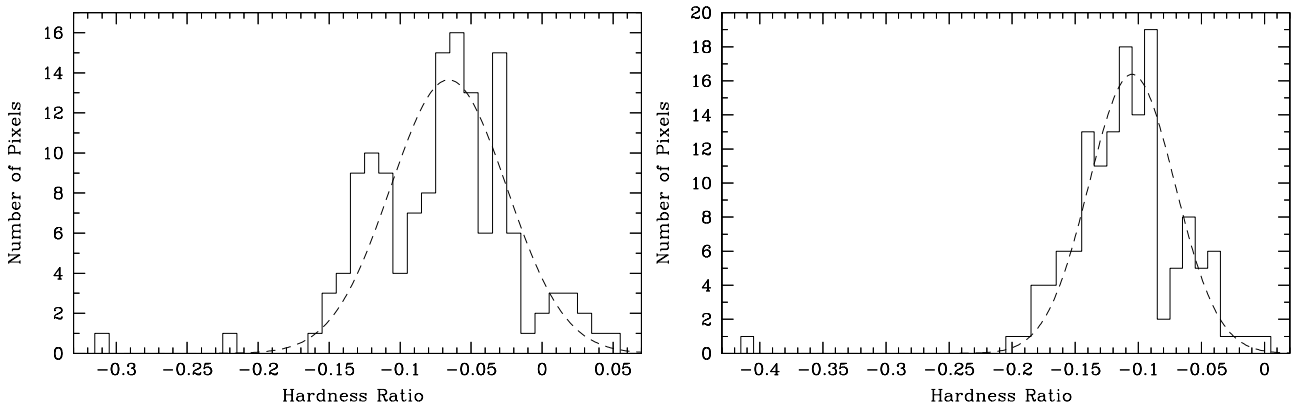

FIG. 8.— Histograms of the hardness ratio for regions b (NGC 4889, left panel) and c (NGC 4874, right panel) of Figure 7. The dashed lines show Gaussians with the same means as the data, but with standard deviations calculated to include only the effect of Poisson noise on the hardness ratio. Apart from a single cool central pixel at the left in each histogram, they are reasonably consistent with a constant hardness ratio in each region.

the X-ray and lensing masses for the two central subhalos is noteworthy. It lends strong support to the interpretation of these mass concentrations as subhalos associated with the two gE galaxies, which lie close to the midplane of the Coma Cluster.

The lack of any significant amount of cool gas associated with the subhalos is consistent with these results. However, more sensitive observations are needed to detect the temperature enhancements that should be caused by adiabatic compression associated with a subhalo. With existing X-ray instruments, the small temperature rise should be more readily detectable in cooler clusters and groups. Apart from providing further constraints on subhalo properties, detecting a temperature rise will help to distinguish gasless subhalos from other sources of X-ray enhancements in clusters (e.g. Churazov et al. 2012).

6. CONCLUSIONS

We have presented an approximate model for calculating the impact of initially gasless subhalos on the X-ray image of a cluster which relies on the subhalos being slow moving and the gas response being adiabatic. The model was applied to *XMM-Newton* and *Chandra* data for the Coma Cluster, using properties determined from lensing data for three central subhalos reported by Okabe et al. (2010). Two of the subhalos correspond to the gE galaxies, NGC 4889 and NGC 4874. When combined with an ellipsoidal model for the gas distribution in the unperturbed cluster, including the effects of these three subhalos produces a model X-ray image that is a much better fit to the observed cluster than the ellipsoidal cluster model alone.

Using the lensing masses for the three subhalos, the distance along our line of sight of each subhalo from the cluster midplane is tightly constrained, with 90% confidence ranges no more than ± 10 kpc ($z_1 = 121 \pm 5$ kpc, $z_2 = 7.9 \pm 7.5$ kpc, and $z_3 = 399 \pm 10$ kpc). The fits are improved considerably when the subhalos associated with the two gE galaxies are assumed to be centered on those galaxies, rather than at the lensing positions, which are consistent within the errors of the lensing determinations. The model favors the subhalos associated with the two gE's lying on the same side of the cluster midplane, further constraining their locations in three dimensions. The results also show the potential for using X-ray images to constrain the internal structure of the two central subhalos.

For each of the two gE galaxies, freeing the total mass of the subhalo gave a significantly better fit ($\Delta\chi^2 \simeq$

240). For the NGC 4889 subhalo, the best fitting mass is 9.1×10^{12} $M_\odot$ ($\simeq$ 1.2 standard deviations smaller than the lensing mass of Okabe et al. 2010), while, for NGC 4874, the best fit is 7.6×10^{12} $M_\odot$ ($\simeq$ 0.9 standard deviations more than the lensing mass). Formally, the X-ray masses are much better determined, although the results are dominated by systematic uncertainties that can only be circumvented with more accurate models. The X-ray and lensing mass determinations rely on completely independent data, so that the agreement between them supports the assumptions that underlie both, most critically that these two subhalos reside near the center of the Coma Cluster. Fitting the X-ray image does not determine a mass for the third subhalo, suggesting that our model assumptions may be less accurate for it.

Our results highlight the potential for using high quality X-ray data to probe substructure in galaxy clusters. Particularly when used in combination with lensing measurements to constrain the mass of a subhalo, X-ray data can constrain where along our line of sight a subhalo lies within a cluster. The X-ray data can also be used to determine subhalo masses and, potentially, to probe their internal structure, i.e., their truncation and scale radii.

We thank R. Johnson for useful discussions. The work was supported in part by Chandra grant AR7-8013X, NASA grant NAS8-03060, FAPESP grant 2008/05970-0, and NASA grant NNX11AF76G.

REFERENCES

Adami, C., Biviano, A., Durret, F., & Mazure, A. 2005, A&A, 443, 17
Arnaud, M., Aghanim, N., Gastaud, R., Neumann, D. M., Lumb, D., Briel, U., Altieri, B., Ghizzardi, S., Mittaz, J., Sasseen, T. P., & Vestrand, W. T. 2001, A&A, 365, L67
Bevington, P. R. & Robinson, D. K. 2003, Data Reduction and Error Analysis for the Physical Sciences (3rd ed.; Boston: McGraw-Hill)
Biviano, A., Durret, F., Gerbal, D., Le Fevre, O., Lobo, C., Mazure, A., & Slezak, E. 1996, A&A, 311, 95
Boylan-Kolchin, M., Springel, V., White, S. D. M., Jenkins, A., & Lemson, G. 2009, MNRAS, 398, 1150
Briel, U. G., Henry, J. P., & Boehringer, H. 1992, A&A, 259, L31
Briel, U. G., Henry, J. P., Lumb, D. H., Arnaud, M., Neumann, D., Aghanim, N., Gastaud, R., Mittaz, J. P. D., Sasseen, T. P., & Vestrand, W. T. 2001, A&A, 365, L60
Brown, S. & Rudnick, L. 2011, MNRAS, 412, 2
Churazov, E., Vikhlinin, A., Zhuravleva, I., Schekochihin, A., Parrish, I., Sunyaev, R., Forman, W., Böhringer, H., & Randall, S. 2012, MNRAS, 421, 1123
Colless, M. & Dunn, A. M. 1996, ApJ, 458, 435
Fakhouri, O., Ma, C.-P., & Boylan-Kolchin, M. 2010, MNRAS, 406, 2267
Fitchett, M. & Webster, R. 1987, ApJ, 317, 653
Gerhard, O., Arnaboldi, M., Freeman, K. C., Okamura, S., Kashikawa, N., & Yasuda, N. 2007, A&A, 468, 815
Giocoli, C., Tormen, G., Sheth, R. K., & van den Bosch, F. C. 2010, MNRAS, 404, 502
Klypin, A., Kravtsov, A. V., Valenzuela, O., & Prada, F. 1999, ApJ, 522, 82
Kubo, J. M., Stebbins, A., Annis, J., Dell'Antonio, I. P., Lin, H., Khiabanian, H., & Frieman, J. A. 2007, ApJ, 671, 1466
Machacek, M. E., Nulsen, P., Stirbat, L., Jones, C., & Forman, W. R. 2005, ApJ, 630, 280
Mandelbaum, R., Seljak, U., & Hirata, C. M. 2008, JCAP, 8, 6
Markevitch, M., Mazzotta, P., Vikhlinin, A., Burke, D., Butt, Y., David, L., Donnelly, H., Forman, W. R., Harris, D., Kim, D.-W., Virani, S., & Vrtilek, J. 2003, ApJ, 586, L19
Mellier, Y., Mathez, G., Mazure, A., Chauvineau, B., & Proust, D. 1988, A&A, 199, 67
Moore, B., Ghigna, S., Governato, F., Lake, G., Quinn, T., Stadel, J., & Tozzi, P. 1999, ApJ, 524, L19
Narayan, R. & Medvedev, M. V. 2001, ApJ, 562, L129
Navarro, J. F., Frenk, C. S., & White, S. D. M. 1997, ApJ, 490, 493
Neumann, D. M., Lumb, D. H., Pratt, G. W., & Briel, U. G. 2003, A&A, 400, 811
Okabe, N., Okura, Y., & Futamase, T. 2010, ApJ, 713, 291
Rocha, M., Peter, A. H. G., Bullock, J. S., Kaplinghat, M., Garrison-Kimmel, S., Oñorbe, J., & Moustakas, L. A. 2013, MNRAS, 430, 81
Springel, V., White, S. D. M., Jenkins, A., Frenk, C. S., Yoshida, N., Gao, L., Navarro, J., Thacker, R., Croton, D., Helly, J., Peacock, J. A., Cole, S., Thomas, P., Couchman, H., Evrard, A., Colberg, J., & Pearce, F. 2005, Nature, 435, 629
Vikhlinin, A., Forman, W., & Jones, C. 1994, ApJ, 435, 162
—. 1997, ApJ, 474, L7
Vikhlinin, A., Markevitch, M., Forman, W., & Jones, C. 2001, ApJ, 555, L87
White, S. D. M., Briel, U. G., & Henry, J. P. 1993, MNRAS, 261, L8

APPENDIX

LIMITS OF THE APPROXIMATIONS

Two conditions must be satisfied in order for the approximations used here to be valid. First, gas displacements caused by a subhalo need to be small compared to the scale of entropy variations in the unperturbed atmosphere for the perturbed gas to be treated as isentropic (Section 3.1). Second, for the fluid acceleration, $d\mathbf{v}/dt$ of Equation (1), to be negligible, it must be small compared to the gravitational acceleration due to the subhalo, $\nabla\delta\Phi$. Here, we determine conditions for these approximations to hold.

The first condition will be satisfied if displacements are small compared to the core radius, $R_{\rm c}$, of the unperturbed atmosphere (Equation (8)). We can estimate the displacements caused by a slowly moving subhalo embedded in isentropic gas from the requirements of mass conservation. Assuming that displacements around a subhalo are radial with respect to the center of the subhalo, the mass of gas within any sphere fixed to the fluid elements of the gas is fixed. In the notation of Section 3.1, conservation of mass therefore requires

$$\frac{4\pi}{3} n_0 r^3 = \int_0^{r-\delta r} n(r') 4\pi r'^2 \, dr', \tag{A1}$$

where the radial coordinates, r and r', are centered on the subhalo and δr is the inward radial displacement of the gas. Using Equation (3) and expanding to first order in the perturbation, this gives

$$\frac{1}{3}n_0[r^3-(r-\delta r)^3] \simeq n_0 r^2 \delta r \simeq \frac{3n_0}{2H_0}\int_0^r [-\delta\Phi(r')]r'^2\,dr'. \tag{A2}$$

Outside the truncation radius, r_t, the gravitational potential for our subhalo model (Section 3.4) is simply $\delta\Phi(r) = -GM_\mathrm{t}/r$, with M_t constant. Although this form overestimates $|\delta\Phi|$, hence δr, for $r < r_\mathrm{t}$, the spherical geometry ensures that the difference it makes to our estimate for δr diminishes rapidly with increasing radius outside r_t. Using $\delta\Phi(r) = -GM_\mathrm{t}/r$ in Equation (A2) to estimate δr (an overestimate), gives

$$\delta r \simeq \frac{3GM_\mathrm{t}}{4H_0}, \tag{A3}$$

independent of r. Although the displacements around a moving halo will not be purely radial, this provides a good estimate for the magnitude of the actual displacements. For the subhalos considered here, $GM_\mathrm{t}/H_0 \ll R_\mathrm{c}$ and the first requirement is well satisfied.

To estimate the fluid accelerations due to a moving subhalo, consider a frame in which the subhalo remains at rest, centered on the origin. At large distances from center of the subhalo, the fluid moves through this frame with velocity $\mathbf{v}_0$, where $-\mathbf{v}_0$ is the velocity of the subhalo with respect to the cluster. In the absence of the subhalo, the path of a fluid element would be given as a function of the time by $\mathbf{r}_0(t) = \mathbf{r}_\mathrm{i} + \mathbf{v}_0 t$, where $\mathbf{r}_\mathrm{i}$ is a constant. Including the approximate radial displacement, δr, of Equation (A3), in the presence of a subhalo the path of the fluid element is given approximately by

$$\mathbf{r}_1(t) = \mathbf{r}_0(t) - \delta r\frac{\mathbf{r}_0(t)}{|\mathbf{r}_0(t)|}. \tag{A4}$$

Differentiating this with respect to the time once gives the fluid velocity

$$\frac{d\mathbf{r}_1(t)}{dt} = \mathbf{v}_0 - \frac{\delta r}{|\mathbf{r}_0(t)|^3}\mathbf{r}_0(t)\times[\mathbf{v}_0\times\mathbf{r}_0(t)], \tag{A5}$$

and twice gives the acceleration

$$\frac{d^2\mathbf{r}_1(t)}{dt^2} = 3\frac{\delta r}{|\mathbf{r}_0(t)|^5}\mathbf{v}_0\cdot\mathbf{r}_0(t)[\mathbf{r}_0(t)\times\{\mathbf{v}_0\times\mathbf{r}_0(t)\}] - \frac{\delta r}{|\mathbf{r}_0(t)|^3}\mathbf{v}_0\times[\mathbf{v}_0\times\mathbf{r}_0(t)]. \tag{A6}$$

In terms of the unit vectors $\widehat{\mathbf{v}}_0 = \mathbf{v}_0/|\mathbf{v}_0|$ and $\widehat{\mathbf{r}}_0(t) = \mathbf{r}_0(t)/|\mathbf{r}_0(t)|$, the cosine of the angle between $\mathbf{v}_0$ and $\mathbf{r}_0(t)$ is $u = \widehat{\mathbf{v}}_0\cdot\widehat{\mathbf{r}}_0(t)$. We then have $|\mathbf{r}_0(t)|^2 = b^2/(1-u^2)$, where b is the distance of closest approach of $\mathbf{r}_0(t)$ to the center of the dark matter halo (the impact parameter of the fluid element). With this notation, the acceleration can be written as

$$\frac{d^2\mathbf{r}_1(t)}{dt^2} = \frac{\delta r}{b^2}|\mathbf{v}_0|^2(1-u^2)\left[2u\widehat{\mathbf{v}}_0 + (1-3u^2)\widehat{\mathbf{r}}_0(t)\right]. \tag{A7}$$

Its magnitude is maximized when $u = 0$, i.e., when the fluid is closest to the center of the subhalo, giving

$$\left|\frac{d^2\mathbf{r}_1}{dt^2}\right|_\mathrm{max} = \frac{\delta r|\mathbf{v}_0|^2}{b^2} \simeq \frac{3GM_\mathrm{t}|\mathbf{v}_0|^2}{4H_0 b^2}. \tag{A8}$$

The gravitational acceleration due to the subhalo at this point is approximately GM_t/b^2, so the requirement that the fluid acceleration be small compared to the gravitational acceleration is simply

$$|\mathbf{v}_0|^2 \ll \frac{4}{3}H_0 = 2s_0^2, \tag{A9}$$

where we have expressed the specific enthalpy in terms of the squared sound speed ($H_0 = 3s_0^2/2$ for $\gamma = 5/3$). This requirement imposes the condition that the speed of the subhalo should be transonic at most.